A Constrained Cylinder Model of Strain Transfer for Packaged Fiber Bragg Grating Sensors Embedded in Inelastic Medium

Ying Huang[1], Yi Bao[2], Genda Chen[3*], F.ASCE, and Zhi Zhou[4]

[1] Department of Civil and Environmental Engineering, North Dakota State University, Fargo, ND

[2] Department of Civil, Environmental and Ocean Engineering, Stevens Institute of Technology, Hoboken, NJ

[3] Department of Civil, Architectural, and Environmental Engineering, Missouri University of Science and Technology, Rolla, MO.

[4] School of Civil Engineering, Dalian University of Technology, Dalian, China

Abstract: In this study, the strain transfer rate from an axially-loaded, inelastic concrete tube to a glass fiber reinforced polymer (GFRP) packaged optical fiber with Bragg gratings is derived when the radial deformation of an "equivalent elastic" concrete tube is constrained by the packaged fiber. The concrete strains, both undisturbed and disturbed by the presence of the fiber Bragg gratings sensor, are analytically evaluated and their difference (up to over *30%*) is related to the development length at two free ends of the GFRP package. The mechanism of strain transfer is dominated by a ratio of average fiber and concrete strains in elastic range, and by the averaging effect and a ratio of disturbed and undisturbed concrete strains in inelastic range. The analytical strain transfer rate was significantly reduced from *0.95*, when concrete behaved elastically, to less than *0.4*, when concrete damaged severely. This result was experimentally validated with less than *10%* difference prior to concrete fracture. The validated model is applicable to fiber optic sensors that are embedded into concrete structures by a concrete cover of at least *10* times of the radius of the optic fiber.

Keywords: Fiber Bragg gratings sensor; Glass fiber reinforced polymer package; Concrete plasticity; Strain transfer; Development length; Sensor-medium interaction

INTRODUCTION

As high-consequence extreme events, such as the 2008 China, 2010 Chile, and 2011 Japan Earthquakes, occurred more frequently, the structural safety of critical constructed facilities has recently been brought to the forefront of most research activities worldwide. In this case, structures often experience large strain and inelastic deformation. For the purpose of safety assessment, the measurement of large strains becomes increasingly important.

Since 1989, fiber optic sensors have been extensively studied due to their unique characteristics such as high sensitivity, high accuracy, corrosion resistance, immunity to electromagnetic interference, and ability for distributed measurement (Morey 1989). To improve its ruggedness in various applications, a Fiber Bragg Gratings (FBG) sensor must be packaged with one or more coating layers. Due to presence of the package layer(s), the strain measured by the fiber optic sensor is less than that in surrounding host materials. This is known as the effect of strain transfer.

Pak (1992) conducted an analytical study on the strain transfer of a coated fiber optic sensor embedded in host composite matrix based on the mechanics of elasticity. The host matrix was assumed to be infinite and subjected to a far-field longitudinal shear load parallel to the optical and structural fibers. Closed-form solutions for the strain and strain transfer distributions were derived in idealized conditions and were experimentally validated by Sirkis and Haslach (1991). The derived strain transfer rate was related to the coating's thickness and the Young's Modulus ratio between the coating and the matrix. Cox (1952) carried out a theoretical analysis of the load transfer from a matrix to the fiber embedded in it, namely shear-lag theory. Based on the shear-lag theory, Ansari and Yuan (1998) proposed a simple strain transfer model for a coated optical fiber embedded in host matrix and experimentally validated the model using a white light Michelson interferometric sensor. They assumed that all materials were linearly elastic and perfectly bonded at their interfaces, and the optical fiber and the matrix were subjected to an equal strain change rate at the middle of the sensor. They found that the strain transfer rate was influenced by the mechanical properties of the coating material and the sensor length. The study by Ansari and Yuan (1998) was extended to take into account the elastoplastic properties of coating materials (Li et al. 2002). The effect of coating behaviors (elastic, elastoplastic, plastic, and post-plastic) on the strain transfer rate was investigated and experimentally validated using a white light Michelson interferometric sensor. By lifting the equal strain change rate assumption between the matrix and its embedded FBG sensor with multilayer coatings at the middle of the sensor, Zhou et al. (2007) generalized the strain transfer model and concluded that the strain transfer rate fell in the range of *0.90~0.95* based on extensive parametric analyses. Li et al. (2007) investigated the strain transfer model of FBG sensors in host matrix under non-axial stress conditions. They found that the sensor orientation could change the strain transfer rate from 0.90 to 0.92. Strain transfer behaviors of long-gauge FBG sensors and distributed sensors were quantitatively studied and implemented in condition monitoring (Glisic et al. 2007; Glisic and Yao 2012; Calderon and Glisic 2012). In the last decade, the strain transfer rate of fiber optic sensors in asphalt pavements has been intensively investigated by Wang et al. (2014, 2016, 2018). Based on the previous understandings on strain transfer, fiber optic sensors have been applied to measure strains and detect damages in various civil engineering structures (Bao et al. 2016, 2017; Bursi et al. 2016; Lan et al. 2014; Sbarufatti et al. 2014).

The influence of the mechanical properties of multi-layer host matrix on the strain transfer from the matrix to an embedded FBG sensor was first considered by Ling et al. (2005) under uniform strain fields. The strain transfer model was developed by finite element analysis, taking into account the effect of the multi-layer host matrix. In this case, the FBG sensor revealed a broadened reflection spectrum or even with multiple peaks, which was different from a single

sharp peak observed under uniform strain fields. Li et al. (2009) further investigated the effect of various host materials on the strain transfer rate from the host matrix to its embedded coated FBG sensor. They showed that the strain transfer rate was approximately *0.95~0.96* and significantly affected by the mechanical properties of the host matrix (Young's Modulus, shear modulus, and Poisson's ratio), the thickness of the sensor coating, and the length of the sensor. The shear-lag theory widely used in the strain transfer model from a host matrix to its embedded optical fiber sensor was challenged in early development stage by Jiang et al. (1998). Instead of solely considering the strain transfer from the matrix to the sensor, they suggested that the influence of the embedded fiber on the mechanical response of the host matrix be taken into account.

The above review indicated that the previous studies have four shortcomings. First, the strain transfer rate from the elastic host matrix to the embedded FBG ranged from *0.90* to *0.96*. These results reflected the practically-insignificant strain transfer problem since a good sensor design for an elastic host matrix naturally resulted in minimum interference on the strain in the host matrix to be measured and thus a constant strain transfer rate slightly less than *1.0*. Only when the stiffness of the matrix changes significantly from the elastic to inelastic state, can the strain transfer rate of the FBG sensor designed for elastic materials be significantly less than *1.0* and practically significant. Second, although the influence of the mechanical properties of host matrix on strain transfer rate was considered in some models, the potential interference of the embedded fiber optical sensor on the strain field in the host matrix was neglected in most studies, which is not justifiable as the host matrix is softened. More importantly, although the strain in optical fiber except at the middle of gratings is transferred from the host matrix by shear, the shear-lag effect may be less significant, particularly near the gratings, since there is no clear eccentricity in load path from the host matrix to the fiber. Third, most, if not all, the derived solutions did not completely satisfy the principle of engineering mechanics, resulting in an unclear mechanism for strain transfer. For example, the compatibility condition between the FBG and the host matrix is often violated. Finally, many assumptions made during the analytical derivation were not validated with experimental results. The small difference between *1.0* and a theoretically-predicted strain transfer rate of *0.90-0.96* can be smeared by random variations in measurement during physical experiments.

In this study, the fundamentals of engineering mechanics are first applied to develop a simple strain transfer model from an axially-loaded concrete cylinder to a FBG sensor packaged with glass fiber reinforced polymer (GFRP) and placed along the centerline of the concrete cylinder. The strain transfer rate is analytically formulated, taking into account the inelastic behavior of concrete. The concrete strains, either undisturbed or disturbed by the presence of the optical fiber, are evaluated from the strain transfer rate. A finite element model of the concrete cylinder is then established and analyzed to understand the mechanism of strain transfer in inelastic medium and validate various assumptions about radial/longitudinal distributions of axial/shear strains made in the simple analytical model of strain transfer. Next, the analytical solution is validated by test results taken from two concrete cylinders. Finally, the applicability of the developed strain transfer model based on axially-loaded cylinders into other concrete members is discussed.

PROBLEM STATEMENT

Consider a general cylinder subjected to an axial compression load as shown in Fig. 1(a). It consists of a thick-walled concrete tube with outer diameter ($2r_m$), a thin-walled GFRP tube of outer diameter ($2r_p$), and an optical fiber of outer diameter ($2r_f$) with one FBG sensor. The sensor with a grating length of l_f is packaged with the GFRP tube over a finite length of L, embedded in

the concrete along the centerline of the cylinder, and connected to an optical spectrum interrogator (OSI) through a light transmission optical fiber that is unbonded with the concrete from the end of the GFRP tube. The OSI and the transmission fiber are not shown in Fig. 1 for clarity. Due to axis-symmetry, half of the longitudinal cylinder section in *r-z* plane is shown in Fig. 1(b) with upward *z* axis originated at the middle of the cylinder. Sections 1-1, 3-3, and 4-4 represent the middle cross section of the cylinders and the FBG sensor, the end cross section of the GFRP tube, and the end cross section of the thick-walled concrete tube. Section 2-2 represents an arbitrary cross section of the cylinder and the GFRP-packaged sensor. The thick-walled concrete tube is subjected to a uniform compressive stress of σ_0 at Section 4-4 or approximately σ_0 at Section 3-3.

The main outcomes of this study include a simple model and mechanism of strain transfer from the concrete tube to the GFRP-packaged FBG sensor, an analytically-formulated strain transfer rate with experimental validations, and an evaluation approach of the undisturbed axial strain in the concrete tube based on the sensor measurement. In the following derivation, three assumptions are made:

1) The thick-walled concrete tube, thin-walled GFRP tube, and optical fiber with an FBG sensor are perfectly bonded at their interfaces.
2) When $r_p/r_m \leq 0.1$, the axial stresses at Section 2-2 are uniform in the thick-walled concrete tube and the GFRP-packaged FBG sensor, respectively.
3) The concrete tube is subjected to inelastic deformation while both the FBG sensor and GFRP tube remain elastic.

According to the plastic deformation theory (Dill 2006), the constitutive law of concrete (Carreira and Chu 1985) can be expressed into:

$$\sigma_m = E_{i^{\sim}} \varepsilon_m - E_m[1 - w(\varepsilon_m)]\varepsilon_m = \frac{\beta(\varepsilon_m / \varepsilon_m')\, f_m'}{\beta - 1 + (\varepsilon_m / \varepsilon_m')^{\beta}} \tag{1}$$

in which σ_m and ε_m denote the stress and strain in concrete, respectively; f_m' and ε_m' are the compressive strength of concrete and its corresponding strain; β is a function of f_m' and ε_m' as well as the initial Young's Modulus of concrete, E_m; $E_{i^{\sim}}$ illustrates the Young's Modulus of the damaged concrete; and $w(\varepsilon_m)$ is a damage function of the concrete. The constant β can be determined from:

$$(0.4\frac{f_m'}{E_m \varepsilon_m'})^{\beta} - \beta(\frac{f_m'}{E_m \varepsilon_m'} - 1) - 1 = 0 \tag{2}$$

The damage function can be written into:

$$w(\varepsilon_m) = 1 - \frac{\beta(f_m' / E_m \varepsilon_m')}{\beta - 1 + (\varepsilon_m / \varepsilon_m')^{\beta}} \geq 0 \tag{3}$$

MECHANICAL MODEL OF STRAIN TRANSFER

As seen from numerical simulations to be presented later, embedding a FBG sensor into a cylinder has little effect on the strain distribution in the cylinder when $r_p/r_m \leq 0.1$. As such, the FBG sensor and its packaging GFRP tube are considered to act like a composite section. Together, they are attached to the thick-walled concrete tube as a constraint layer to the axial deformation in the concrete. For the GFRP-FBG composite section, the elastic stress-strain relationships of the GFRP and FBG materials are $\sigma_p(z) = E_p \varepsilon_p(z)$ and $\sigma_f(z) = E_f \varepsilon_f(z)$, in which E_p and E_f represent

the Young's Modulus of the GFRP tube and the optical fiber, respectively; and the strain in the GFRP tube, $\varepsilon_p(z)$, and the strain in the FBG sensor, $\varepsilon_f(z)$, are considered equal. In this case, the Young's Modulus of the composite section is equal to $E_p(1-r_f^2/r_p^2)+E_f r_f^2/r_p^2 \approx E_p$ when $r_f/r_p \le 0.1$, and E_p and E_f are in the same order. In other words, the material property of the composite section is dominated by that of the GFRP tube. For this reason, the Poisson ratio of the GFRP tube υ_p is used for the composite section.

Radial Displacement Compatibility for Strain Transfer Rate Formulation

As stated in the third assumption, the concrete tube under axial loading in compression as shown in Fig. 1 is subjected to inelastic deformation while the GFRP tube and the optical fiber with one FBG sensor remain elastic. For simplicity, however, the concrete tube is treated as an elastic material with the Young's Modulus E_m under an axial stress equivalent to inelastic strain as expressed in Eq. (1). In this case, the stress field near *z=0* remains unchanged over the length of the cylinder. The inner surface of the "equivalent elastic" thick-walled concrete tube and the outer surface of the elastic composite section expand together in radial direction. The radial expansions of the concrete tube and the composite section near *z=0* can be respectively calculated by (Young 1989):

$$\Delta r^{(m)}(0) = \frac{\sigma_m(0)\upsilon_m r_p r_m^2}{E_m(r_m^2 - r_p^2)}, \quad \Delta r^{(c)}(0) = \frac{\sigma_p(0)\upsilon_p r_p}{E_p} \tag{4}$$

where υ_m is the Poisson ratio of concrete, and $\sigma_m(0)$ and $\sigma_p(0)$ are the longitudinal/axial stresses of the concrete and the composite section, respectively. For perfect interface bonding as stated in the first assumption, the radial expansion $\Delta r^{(m)}(0)$ at the inner surface of the thick-walled concrete tube must be equal to $\Delta r^{(c)}(0)$ at the outer surface of the composite section. This equality leads to the strain transfer rate η_a near *z=0* or the strain ratio between the composite section and the concrete:

$$\eta_a = \eta_e\{1 - w[\varepsilon_m(0)]\}, \ \eta_e = \frac{\upsilon_m}{\upsilon_p[1-(r_p/r_m)^2]} \le 1 \tag{5}$$

after $\sigma_m(0) = E_i \varepsilon_m(0)$ and $\sigma_p(0) = E_p\varepsilon_p(0)$ have been introduced. The quantity η_e in Eq. (5) represents the maximum strain transfer achieved when the concrete remains elastic or the damage function is set to zero, which is bounded by *1.0* since the strain in optical fiber is induced from the applied stress in concrete by shear effect at their interface. For normal weight concrete, the Poisson ratio is approximately *0.2* but likely increases as inelastic deformation is developed under compression. For example, Yaman et al. (2002) found that $\upsilon_m \approx 0.228$ considering active and non-active porosity in concrete. For the orthotropic GFRP packaging material, $\upsilon_p \approx 0.25 \sim 0.35$ when the glass fibers are aligned with the loading direction (Dickerson and Di Martino 1966). Therefore, $\eta_e \approx 0.66 \sim 0.92$ when $r_p/r_m = 0.1$. The upper bound (*0.92*) lies between *0.90* and *0.96* as reported by other investigators (Li et al. 2006, 2009, Zhou et al. 2007). In the following analysis, however, $\eta_e = 0.95$ is used as it is calibrated well with experimental data in the elastic range of concrete behavior as will be discussed later.

Equations of Equilibrium for Shear Transfer Mechanism

The free-body diagram of an infinitesimal element *dz* of each of the three layers in Fig. 1 is shown in Fig. 2 (only horizontal forces shown for clarity). Here, $\sigma_f(z)$ represents the axial stress applied at location *z* of the optical fiber. Due to the transferred shear stress through the GFRP tube, the axial stresses on the optical fiber and the concrete tube are uniformly distributed over their cross sections as illustrated in Fig. 2 according to the second assumption.

Due to no external load applied over the *dz* length in Fig. 2, the total change in longitudinal forces of the concrete tube, GFRP tube, and optical fiber must be zero between any two sections in Fig. 2 and can be written as:

$$r_f^2 \frac{d\sigma_f(z)}{dx} + (r_p^2 - r_f^2)\frac{d\sigma_p(z)}{dz} + (r_m^2 - r_p^2)\frac{d\sigma_m(z)}{dz} = 0 \tag{6}$$

By integrating both sides of Eq. (6) over *z* and introducing the boundary conditions at *z=L/2*, $\sigma_p(L/2) = \sigma_f(L/2) = 0$ and $\sigma_m(L/2) = \sigma_0$, Eq. (6) becomes:

$$r_f^2\sigma_f(z) + (r_p^2 - r_f^2)\sigma_p(z) = (r_m^2 - r_p^2)[\sigma_0 - \sigma_m(z)] \tag{7}$$

Note that Eq. (7) is valid for both the elastic and inelastic behavior of concrete.

For the axisymmetric problem about the centerline of the optical fiber, the shear stress along the perimeter of the optical fiber is the same. The equation of force equilibrium over the length *dz* of the optical fiber leads to:

$$\tau_f\left(z, r_f\right) = -\frac{r_f}{2}\frac{d\sigma_f(z)}{dz} \tag{8}$$

in which $\tau_f\left(z, r_f\right)$ is the shear stress at $r=r_f$. Similarly, the force equilibrium over the length *dz* of the concrete with radius from $r = r_p$ to $r = r_m$ results in:

$$\tau_m\left(z, r_p\right) = \frac{r_m^2 - r_p^2}{2r_p}\frac{d\sigma_m(z)}{dz} \tag{9}$$

in which $\tau_m\left(z, r_p\right)$ is the shear stress at $r=r_p$. Note that the zero shear stress on the outer surface of the concrete tube was introduced in the derivation of Eq. (9).

For the packaging layer, an infinitesimal element *dz* is taken with radius from *r* to *r+dr* as shown in Fig. 3. Both the shear stress $\tau_p\left(z, r\right)$ and the axial stress $\sigma_p(z)$ are included in Fig. 3. The longitudinal force equilibrium over the element *dz* gives the following equation:

$$\tau_p\left(z, r\right) + r\frac{\partial\tau_p\left(z, r\right)}{\partial r} + r\frac{d\sigma_p(z)}{dz} = 0\,. \tag{10}$$

The solution of Eq. (10) with boundary conditions $\tau_p\left(z, r_f\right) = \tau_f(z, r_f)$ and $\tau_p\left(z, r_p\right) = \tau_m(z, r_p)$ taken at $r = r_f$ and $r = r_p$ can be expressed into:

$$\tau_p(z, r) = \frac{r_p^2 - r^2}{2r}\frac{d\sigma_p(z)}{dz} + \frac{r_m^2 - r_p^2}{2r}\frac{d\sigma_m(z)}{dz} \tag{11}$$

after Eq. (8) and Eq. (9) have been introduced.

Disturbed and Undisturbed Strains in Host Matrix and the Applied Stress σ_0

Each of the three layers (concrete, GFRP, and FBG) is mainly subjected to axial

deformation. After the stress-strain relations of the three layers and $\varepsilon_p(z) = \varepsilon_f(z)$ in a composite section of optical fiber and package layer have been introduced, Eq. (7) can be rewritten into:

$$\sigma_0 = E_m \varepsilon_m(z)\{1 - w[\varepsilon_m(z)]\} + [r_f^2 E_f + (r_p^2 - r_f^2)E_p]\varepsilon_f(z) / \left(r_m^2 - r_p^2\right) \quad (12)$$

Therefore, the applied stress σ_0 is composed of two parts: one on the thick-walled concrete tube and the other on the composite section.

The strains at z=0 and z=L/2, $\varepsilon_m(0)$ and $\varepsilon_m(L/2)$, are respectively defined as the disturbed and undisturbed strains in concrete associated with the presence of the FBG sensor. In applications, σ_0 is unknown and only the strain $\varepsilon_f(0)$ measured from the FBG sensor is available. When η_a is directly related to the concrete strain at *z=0*, the disturbed and undisturbed strains in concrete can be evaluated according to the following four-step procedure:

1) Select an initial strain in concrete $\varepsilon_m^{(i)}(0)$ at *z=0*.
2) Calculate the strain transfer rate from Eq. (5) corresponding to $\varepsilon_m^{(i)}(0)$, termed as $\eta_a^{(i)}$. With the measured strain from the FBG sensor, a new strain in the concrete can be determined by $\varepsilon_m^{(i+1)}(0) = \varepsilon_f(0) / \eta_a^{(i)}$.
3) Repeat Steps 1 and 2 with *i* replaced by (*i+1*) unless $\left|\varepsilon_m^{(i+1)}(0) - \varepsilon_m^{(i)}(0)\right| \Big/ \varepsilon_m^{(i)}(0) \le e$, where *e* (e.g. 5%) is a predetermined acceptable error. Note that, if $\eta_a^{(i)} = 1$, $\varepsilon_m^{(i)}(0) = \varepsilon_f(0)$.
4) Evaluate σ_0 from Eq. (12) with the measured $\varepsilon_f(0)$ and the calculated $\varepsilon_m^{(i+1)}(0)$ at *z=0*. The undisturbed strain in the concrete is then determined from $E_m \varepsilon_m(L/2)[1 - w(\varepsilon_m(L/2)] = \sigma_0$. Given σ_0, the undisturbed strain is a function of the damage function of the concrete, which in turn is a function of the strain to be determined. Unless the concrete behaves elastically when the damage function is zero, iterations must be taken to evaluate the undisturbed strain.

NUMERICAL VERIFICATION AND SENSITIVITY ANALYSIS

Since the strain from each FBG sensor is measured over a very short grating length (e.g. l_f = *2 mm*), the analytical strain transfer rate at *z=0*, η_a in Eq. (5), can be used to relate the FBG measurement to the strain in concrete. Even so, the strain of the 'equivalent elastic" concrete tube near *z=0*, $\varepsilon_m(0)$ in Eq. (5), represents a certain average effect of the stress field over the length of GFRP tube. Therefore, to understand the longitudinal distribution of strains in concrete tube, GFRP tube, and optical fiber becomes a critical step towards the understanding of underlying mechanism of Eq. (5), the determination of an applicable range (*z*) of Eq. (5), and an appropriate length of the GFRP package tube in sensor design.

Furthermore, when the proposed analytical model of strain transfer is applied into general RC structures, the diameter ($2r_m$) of a "virtual" cylinder must be selected for an appropriate evaluation of strain transfer rate. This can only be accomplished by understanding the radial distribution of axial strains of the concrete tube. The second assumption about the stress distribution over Section 2-2 must also be justified. In addition, for the design of sensors and their package, the development length of packaged sensors must be determined. Therefore, parametric studies with a finite element model of the cylinder were conducted with various r_p/r_m ratios,

package lengths (L) of a FBG sensor, and loading levels (σ_0).

Concrete Cylinders and Material Properties

Consider a *200 mm* tall concrete cylinder with an embedded GFRP-packaged FBG sensor. The constitutive law of concrete under compression is given in Eq. (1). The material properties of 28-day concrete are: $f_m' = 20\,MPa$, $\varepsilon_m' = 0.0019$, $\beta = 2$, and $E_m = 21GPa$ (Dill 2006). These properties correspond to the upper-bound strain (0.000095) for linear behavior of the concrete cylinder when the damage function in Eq. (3) is set to zero. The packaging GFRP tube (r_p = 1.5 *mm*) and the optical fiber (r_f = 62.5 μm) have a Young's modulus of $E_p = 50\,GPa$ and $E_f = 70\,GPa$, respectively. The Poisson ratios of the concrete and GFRP are taken to be $\upsilon_m = 0.235$ and $\upsilon_p = 0.25$, respectively, so that η_e in Eq. (5) is equal to *0.95*. Fig. 4(a) shows the stress-strain relationship of the concrete and the GFRP. It can be seen from Fig. 4(a) that, as the concrete experiences plastic damage, a small increase in stress will induce a large change in strain. However, the stiffer packaging material, GFRP, remains elastic till fracture. The strain difference between the two materials will increase dramatically with the increase of the plastic deformation in the concrete. Fig. 4(b) illustrates the corresponding damage function of the concrete as strain increases. For the *20 MPa* concrete, the damage function $w(\varepsilon_m)$ is equal to *0.55* when $\varepsilon_m = 0.0021$.

Finite Element Model and Strain Distribution

A finite element model of the concrete cylinder was established in ANSYS platform and analyzed in a displacement/strain-controlled manner due to strong nonlinear behavior of concrete material. The model included two long cavities of the concrete tube extending outward from the two ends of the GFRP tube. The concrete tube with its material constitutive law represented by Eq. (1) was modeled using Solid 185 elements. The GFRP package and optical fiber were both modeled using Solid 45 elements. The entire model had *53,000* meshed elements. Due to axis-symmetry, only one quarter of the cylinder was modeled. On the two cut planes, the out-of-plane displacement was restrained. In addition, the middle cross section of the model was also restrained from longitudinal displacement in z direction. Uniform compressive strains were applied on both end faces of the concrete cylinder.

Fig. 5(a) shows the overall distribution of axial strains in the concrete cylinder (r_p/r_m=*0.07* and *L=100 mm*) when subjected to *240 με* (*5 MPa*) at each end. Figs. 5(b) and 5(c) illustrate the longitudinal distributions of axial compressive and interfacial shear strains, respectively, in both the FBG sensor and the concrete cylinder. Figs. 5(d, e) demonstrate the radial distributions of axial compressive and shear strains, respectively, at the four cross sections defined in Fig. 1(b). It can be observed from Fig. 5(a) that the strains in the cylinder are generally uniform unless in the proximity of the two ends of the GFRP tube. This observation is confirmed by the longitudinal and radial distributions of axial strains around the package layer as detailed in Figs. 5(b-e). In particular, the axial strain distributions over all but cross section 3-3 are generally uniform as indicated in Fig. 5(d). By comparing Fig. 5(b) with Fig. 5(c), it can be seen that the first derivative of the axial strain in the concrete tube/FBG sensor with respect to z approximately corresponds to the shear strain in the concrete tube/FBG sensor. This comparison partially verifies the analytical relations in Eq. (8) and Eq. (9). It can also be seen that the longitudinal distribution of axial strain difference between the FBG sensor and the concrete tube as shown in Fig. 5(b) is closely related to that of the shear strain at the FBG-GFRP interface as illustrated in Fig. 5(c), indicating a shear transfer mechanism of strain from the concrete to the FBG sensor.

Parametric Studies

Three parameters were considered: 1) r_p/r_m = *0.2*, *0.1*, and *0.07*; 2) L = *50*, *100*, and *150* mm; and 3) ε_0= *240, 900, 1900,* and *2100* $\mu\varepsilon$ (σ_0 = *5.0, 15.5, 20.0, and 19.9 MPa*). Fig. 6(a) shows the shear strain at cross section 3-3 in Fig. 1(b) when ε_0=*240* $\mu\varepsilon$, L=*100 mm*, r_p=*1.5 mm,* and r_p/r_m = *0.2, 0.1,* and *0.07*. The maximum shear strain occurred at the GFRP-concrete interface and remained nearly the same when the diameter of the concrete cylinder changed. Fig. 6(b) shows the distribution of strain transfer rate for the three r_p/r_m ratios. It can be clearly seen from Fig. 6 that both the shear strain distribution near the FBG sensor and the strain transfer rate remain nearly unchanged when r_p/r_m is less than *0.1*. In other words, when r_p =*1.5 mm*, the strain transfer rate derived from a concrete tube with *1.5 mm* and *15 mm* in inner and outer radius is applicable to other cases when the outer radius exceeds *15 mm*. This requirement can easily be met in engineering practice through the use of concrete cover in RC structures.

Fig. 7 illustrates the change in strain transfer rate distribution for various sensor package lengths of *50, 100*, and *150 mm* with r_p/r_m =0.07 and ε_0=*240* $\mu\varepsilon$. It is seen that the sensor package length has little or no effect on the shape of strain transfer rate curve. For all three sensors with different package lengths, the strain transfer rate is approximately *1.0* at the middle of sensor gratings, remains nearly unchanged over the middle 80% of the package length (L), and then is reduced dramatically to zero towards the end of the package layer. Due to symmetry, the remaining *20%* of half a package length ($L/2$) at each end is referred to as the development length of the packaged sensor required in design. Considering potential debonding at the end of package layer, a design factor of *2* is considered and the minimum package length can be considered as *2.5* times the grating length when the concrete tube experiences nearly elastic behavior.

The effect of loading (corresponding to ε_0= *900, 1900, and 2100* $\mu\varepsilon$) on the longitudinal distribution of strain transfer rate is presented in Fig. 8 when L=*100 mm* and r_p/r_m=*0.07*. It can be observed from Fig. 8 that the development length of the GFRP tube increases from approximately *20%* to *80% (L/2)* as the applied strain increases from *900* to *2100* $\mu\varepsilon$ or the concrete is softened. In this case, the minimum length of the GFRP layer is *10* times the grating length, accounting for a design factor of *2* for potential debonding.

Both the numerical and analytical analyses took into account the nonlinear behavior of concrete such as cracks by introducing a damage function, $w(\varepsilon_m)$, as given in Eq. (3). However, the numerical analysis was based on the three-dimensional (3D) finite element model of concrete cylinder, which allows the understanding of 3D stress/strain distributions and the determination of strain transfer rate at every point along the length of the GFRP package as illustrated in Fig. 8 at three strain levels. The analytical solution of strain transfer rate independent of z, Eq. (5), was developed for a prismatic cylinder with an overall effect of the stress field in concrete tube over the package length L. To understand this overall effect, three indices are calculated from numerical analysis at various applied strains as follows:

$$\eta_1 = \frac{2}{L}\int_0^{L/2} \frac{\varepsilon_f(z)}{\varepsilon_m(z)}dz\ ,\ \eta_2 = \frac{\int_0^{L/2}\varepsilon_f(z)dz}{\int_0^{L/2}\varepsilon_m(z)dz},\ \eta_3 = \frac{\varepsilon_f(0)}{\varepsilon_m(0)} \times \frac{\varepsilon_m(0)}{\varepsilon_m(L/2)} \approx \frac{\varepsilon_m(0)}{\varepsilon_m(L/2)} \qquad (13)$$

The first and second indices in Eq. (13) represent an average of the longitudinal distribution of strain transfer rate, as illustrated in Fig. 8, and a ratio of the averaged strains in FBG sensor and concrete tube, respectively. The third index in Eq. (13) is a formal definition of strain transfer rate, which is a ratio of the sensor measurement and the undisturbed concrete strain. This definition signifies the effect of sensor placement on the change of concrete strain (hereafter referred to as

the disturbance effect) since the strain transfer rate at *z=0* is approximately equal to one as illustrated in Fig. 8. Fig. 9 compares the three indices of stress field effect under various applied strains when *L=100 mm* and $r_p/r_m=0.07$. All the indices clearly indicate a reduced strain transfer rate when the concrete behavior changes from elastic to inelastic. The averaging effects represented by η_1 and η_2 are nearly proportional to each other. In comparison with the averaging effects, the disturbance effect represented by η_3 is significantly more sensitive to the change in large strain. At small strains, the placement of a sensor has little or no effect on the stress distribution in concrete tube.

EXPERIMENTAL VALIDATION OF STRAIN TRANSFER MODEL

Test Setup

To validate the proposed mechanical model of strain transfer considering the plastic damage in host matrix, two concrete cylinders with *50 mm* in diameter and *200 mm* in height were tested. One FBG sensor was embedded along the centerline of and in the middle portion of each concrete cylinder. Fig. 10(a) illustrates the schematic view of each test specimen. The two FBG sensors used in this experiment are shown in Fig. 10(b). For protection, each sensor was packaged with a GFRP layer with 3 mm in diameter. To produce the same boundary condition as shown in Fig. 1, a small PVC tube was bonded to each end of the GFRP-FBG sensor by epoxy in order to make the sensor ends free of stress. One representative cast specimen is presented in Fig. 10(c). On the side face of each cylinder, two 76 mm long strain gauges were installed to measure axial strains of the concrete.

A load frame (MTS2550) was used to apply the axial load on each specimen at a loading rate of *445 N/sec*. The loading process continued until the fracture of the concrete specimen. Data from the FBG sensor were collected by Optical Sensing Interrogator (OSI, Model SM125, Micron Optics, Inc). The strains from both the FBG sensor and electrical resistance strain gauges were recorded at a *1.0 Hz* sampling frequency. Figs. 11(a, b) show the partial test setup and the schematic view of the complete test system, respectively.

Results and Discussion

Two specimens tested were designated as #1 and #2. The stress determined from the applied loading is plotted in Figs. 12(a) and 13(a), respectively, as a function of the strain from the FBG sensor and the average strain measured from the two strain gauges. The stress-strain curves in Figs. 12(a) and 13(a) based on the strain gauge readings were best fitted to estimate the constitutive law parameters: $f_m' = 6.16\,MPa$, $\varepsilon_m' = 0.00028$, $E_m = 25GPa$, and $\beta = 2$ for specimen #2, and $f_m' = 8.06MPa$, $\varepsilon_m' = 0.0004$, $E_m = 22\,GPa$, and $\beta = 2$ for specimen #3. The strain ratio between the FBG sensor and the two strain gauges represents the experimental strain transfer rate, which is presented in Figs. 12(b) and 13(b), respectively, and compared with the analytical strain transfer rate from Eq. (5) using the compressive strengths obtained from the tests. It can be clearly observed from Figs. 12(a) and 13(a) that the strains measured from the strain gauges and the FBG sensor are in excellent agreement when the concrete cylinder behaved elastically, both proportional to the applied loading. The analytical results start to deviate from the measured data once the concrete cracking as illustrated in Fig. 14(a) was initiated. Their difference reached a maximum at concrete fracture as illustrated in Fig. 14(b). As also shown in Figs. 12(b) and 13(b), both the analytical and experimental strain transfer rates are nearly constant in elastic

range and then decay exponentially with the applied loading as concrete is subjected to light to severe damages. Represented by the damage function of concrete, the light damage is related to minor longitudinal cracks in concrete, as shown in Fig. 14(a), and the severe damage is to significant splitting cracks or concrete fracture, as shown in Fig. 14(b). The softened concrete provided a reduced constraint to the embedded FBG sensor. Therefore, the sensor was less strained as additional loads were applied on the concrete. Overall, the maximum difference between the analytical and experimental strain transfer rates prior to concrete fracture is less than *10%*, which validates the proposed mechanical model of strain transfer from the concrete to the embedded FBG sensor.

At the completion of all tests, the two tested specimens were collected as shown in Fig. 14(c). Their fracture failure modes are representative to any concrete cylinder tests and consistent between them under compressive loading. These results ensured the repeatability of the test process and results.

CONCLUSIONS

This paper presents a combined analytical, numerical, and experimental study of strain transfer mechanism from an axially loaded concrete cylinder to an embedded GFRP-packaged FBG sensor. Both elastic and inelastic behaviors of the concrete were considered in the evaluation of strain transfer rate, GFRP package development length, and undisturbed concrete strain. Based on the analysis and experiment, the following conclusions can be drawn:

1) A simple strain transfer model, Eq. (5), was developed based on the radial displacement compatibility between the concrete and its concentric GFRP-packaged optical fiber with Bragg gratings. The undisturbed and disturbed concrete strains by the presence of the fiber optic sensor are related by the longitudinal force equilibrium. The mechanism of strain transfer is dominated at small strains by a ratio of average fiber and concrete strains and, at large strains, by the averaging effect and a ratio of disturbed and undisturbed concrete strains.
2) The strain transfer rate changes with a damage function of the concrete, and geometries and material properties of the concrete and a composite section of the sensor and package. It was approximately *0.95*, independent of external loading when the concrete remained elastic, but exponentially reduced to less than *0.4* as the concrete experienced cracking to fracture mainly through the reduction in Young's modulus. It was validated by experimental results up to concrete fracture with less than *10%* difference.
3) Due to elasticity of the package layer, the strain in the optical fiber became steady beyond a development length that varies from *20%* to *80%* of the package length as the concrete behaves from cracking to fracture under compression. Therefore, it is recommended that the GFRP package length exceed *10* times the grating length of a packaged sensor in practical design, considering a design factor of *2* accounting for potential debonding at the end of GFRP package.
4) When the analytical strain transfer rate is directly related to the concrete strain at $z=0$ (or $z=L/2$), the undisturbed concrete strain can be determined based on the sensor measurement according to the proposed four-step analysis procedure (or directly estimated from a ratio of the sensor measurement and the analytical strain transfer rate). The effect of sensor deployment on the concrete strain can be over *30%*. The undisturbed concrete strain and the experimentally-validated strain transfer model are applicable to RC members and structures where the concrete cover over a packaged

sensor exceeds *10* times the radius of the package layer.

ACKNOWLEDGEMENTS

Financial support for this study was provided in part by the U.S. National Science Foundation under Award No. CMMI-0825942 from Missouri University of Science and Technology and Award No. CMMI-1750316 from North Dakota State University. The findings and opinions expressed in the paper are those of the authors only and do not necessarily reflect the views of the sponsors.

REFERENCES

Ansari, F., and Yuan, L. B. (1998). "Mechanics of bond and interface shear transfer in optical fiber sensors." ASCE *Journal of Engineering Mechanics*, 124(4), 385–394.

Bao, Y., Tang, F., Chen, Y., Meng, W., Huang, Y., and Chen, G. (2016). "Concrete pavement monitoring with PPP-BOTDA distributed strain and crack sensors." *Smart Structures and Systems*, 18(3), 405-423.

Bao, Y., Valipour, M., Meng, W., Khayat, K. H., and Chen, G. (2017). "Distributed fiber optic sensor-enhanced detection and prediction of shrinkage-induced delamination of ultra-high-performance concrete overlay." *Smart Materials and Structures*, 26(8), 085009.

Bursi, O. S., Tondini, N., Fassin, M., and Bonelli, A. (2016). "Structural monitoring for the cyclic behaviour of concrete tunnel lining sections using FBG sensors." *Structural Control and Health Monitoring*, 23(4), 749-763.

Cox, H. L. (1952). "The elasticity and strength of paper and other fibrous materials." *British Journal of Applied Physics*, 3, 72–79.

Calderon, P., Glisic, B. (2012). "Influence of mechanical and geometrical properties of embedded long-gauge strain sensors on the accuracy of strain measurement." *Measurement Science and Technology*, 23(6), 065604.

Carreira, D. J., and Chu, K. H. (1985). "Stress-strain relation for plain concrete in compression." *ACI Materials Journal*, 82(6), 797-804.

Dickerson, E.O., and di Martino, B. (1966). "Off-axis strength and testing of filamentary materials for aircraft application." *Proceedings of the 10th National Symposium, SAMPE*, San Diego, 9-11 November 1966, H23-H50.

Dill, E. H. (2006). *Continuum Mechanism (Elasticity, Plasticity and Visco-elasticity)*, CRC Press, NW.

Glisic, B., Yao, Y. (2012). "Fiber optic method for health assessment of pipelines subjected to earthquake-induced ground movement." *Structural Health Monitoring*, 11(6), 696-711.

Glisic, B., Posenato, D., Inaudi, D. (2007). "Integrity monitoring of old steel bridge using fiber optic distributed sensors based on Brillouin scattering." *Proceedings of SPIE - The International Society for Optical Engineering*, Nondestructive Characterization for Composite Materials, Aerospace Engineering, Civil Infrastructure, and Homeland Security 2007, 6531, 10 pages.

Lan, C., Zhou, Z., and Ou, J. (2014). "Monitoring of structural prestress loss in RC beams by inner distributed Brillouin and fiber Bragg grating sensors on a single optical fiber." *Structural Control and Health Monitoring*, 21(3), 317-330.

Li, H. N., Zhou, G. D., Ren, L., and Li, D. S. (2007). "Strain transfer analysis of embedded fiber Bragg grating sensor under non-axial stress." *Optical Engineering*, 46, 054402.

Li, H. N., Zhou G. D., Ren, L., and Li, D. S. (2009). "Strain transfer coefficient analyses for embedded fiber Bragg grating sensors in different host materials." *ASCE Journal of Engineering Mechanics,* 135, 1343-1353.

Li, J., Zhou, Z., and Ou, J. (2004b). "Interface transferring mechanism and error modification of embedded FBG strain sensor." *Proceedings of SPIE - The International Society for Optical Engineering*, Smart Structures and Materials 2004: Smart Sensor Technology and Measurement Systems, 5384, 9 pages.

Li, Q., Li, G., Wang, G., Ansari, F., and Liu, Q. (2002). "Elasto-plastic bonding of embedded optical fiber sensors in concrete." ASCE *Journal of Engineering Mechanics*, 128, 471–478.

Ling, H., Lau, K., Cheng, L., and Chow, K. (2005). "Embedded fibre Bragg grating sensors for non-uniform strain sensing in composite structures." *Measurement Science Technology*, 16(12), 2415–2424.

Morey, W. W., Meltz, G., Glenn, and W. H. (1989). "Fiber optical Bragg grating sensors." *Proceedings of SPIE - The International Society for Optical Engineering,* Fiber Optic and Laser Sensors VII, 1169, 98-107.

Pak, Y. E. (1992). "Longitudinal shear transfer in fiber optic sensors." *Smart Materials and Structures*, 1, 57–62.

Sbarufatti, C., Manes, A., and Giglio, M. (2014). "Application of sensor technologies for local and distributed structural health monitoring." *Structural Control and Health Monitoring*, 21(7), 1057-1083.

Sirkis, J. S., and Haslach, Jr. H. W. (1991). "Complete phase strain model for structurally embedded interferometric optical sensors." *Journal of Intelligent Material Systems and Structures*, 2(1), 3-24.

Wang, H. P. and Zhou, Z. (2014). "Advances of strain transfer analysis of optical fibre sensors." *Pacific Science Review*, 16(1), 8-18.

Wang, H. P. and Xiang, P. (2016). "Strain transfer analysis of optical fiber based sensors embedded in an asphalt pavement structure." *Measurement Science and Technology*, 27, 075106.

Wang, H. P., Jiang, L. and Xiang, P. (2018). **"**Improving the durability of the optical fiber sensor based on strain transfer analysis." *Optical Fiber Technology*, 42, 97.

Yaman, I.O., Hearn, N., and Aktan, H.M. (2002). "Active and non-active porosity in concrete part I: experimental evidence." *Materials and Structures*, 35, 102-109.

Young, W. C. (1989). *Roark's Formulas for Stress & Strain*, 6th Edition, McGraw-Hill, Inc.

Zhou, Z., Li, J. L., and Ou, J. P. (2007a). "Interface transferring mechanism and error modification of embedded FBG strain sensor." *Frontiers of Electrical and Electronic Engineering in China*, 2(1), 92-98.

List of Figure Captions

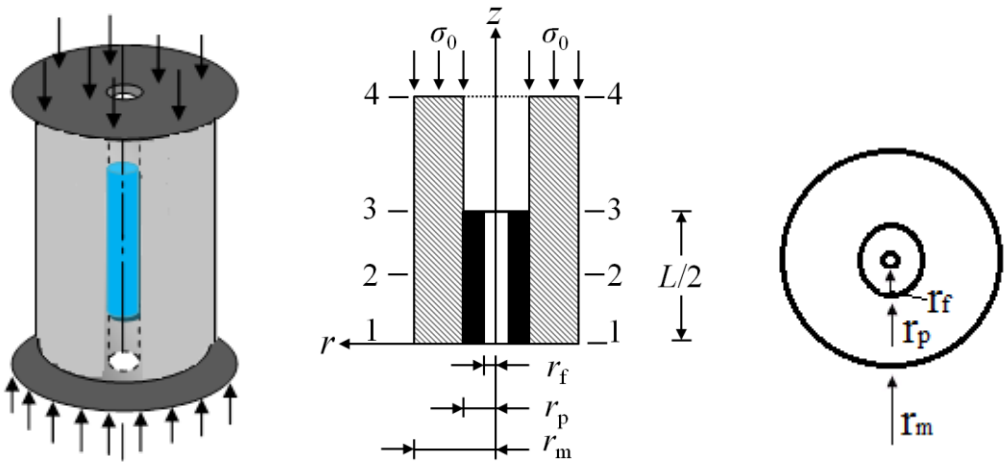

(a) Axially loaded cylinder (b) Half of the longitudinal section (c) Cross section at 2-2

Fig. 1 Schematic view of thick-walled concrete, thin-walled GFRP, and FBG sensor

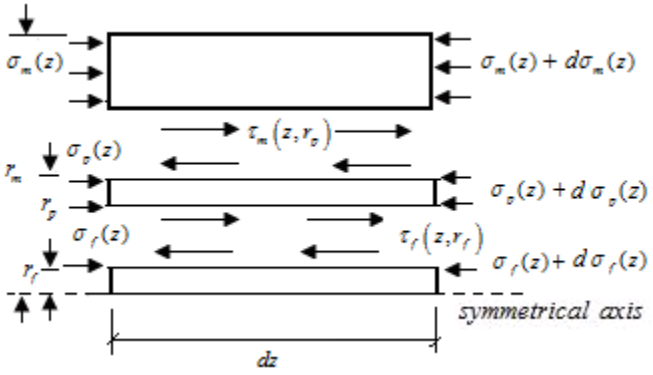

Fig. 2 Shear stress transfer among various layers

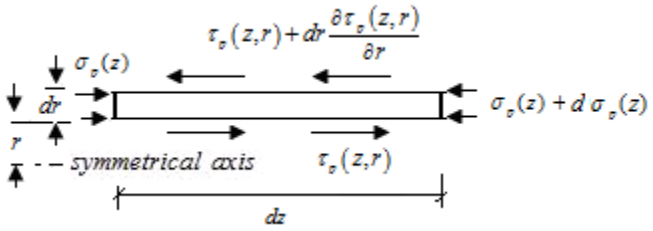

Fig. 3 Free-body diagram of an infinitesimal element of the package layer

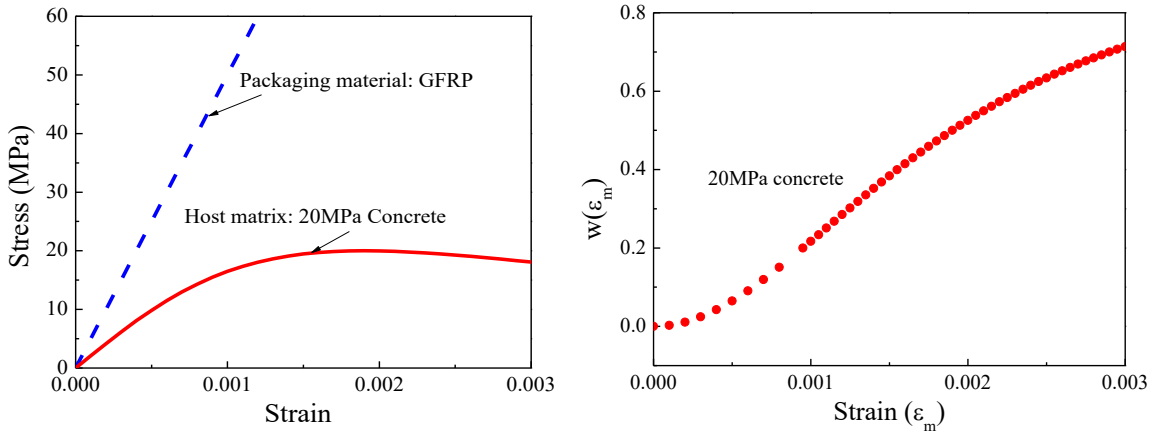

(a) Stress-strain relations of concrete and GFRP (b) Damage function of concrete

Fig. 4 Constitutive laws and damage function

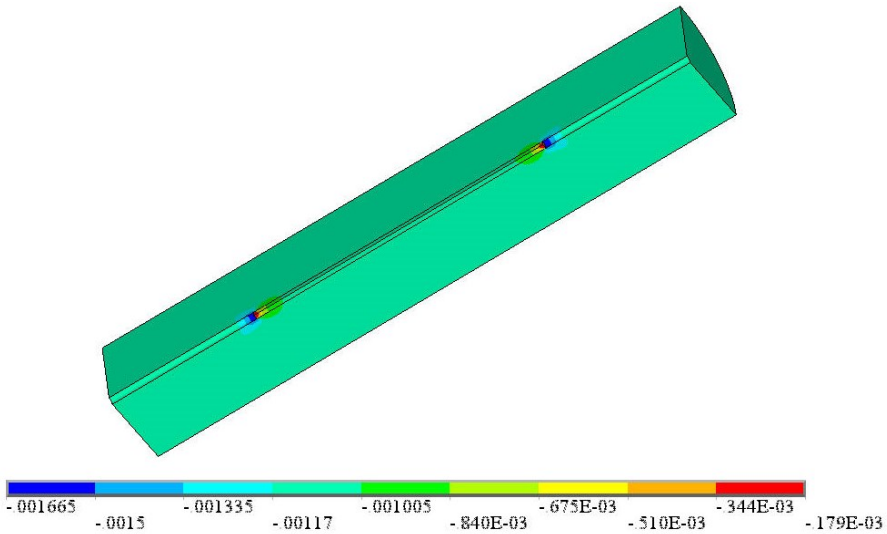

(a) Axial strain field

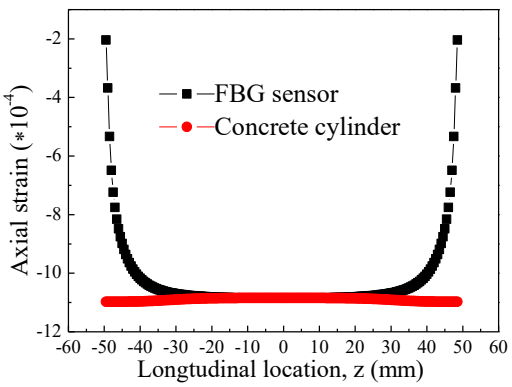

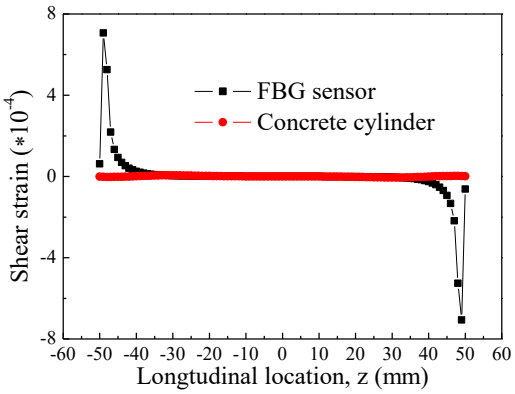

(b) Axial strains in FBG sensor and concrete cylinder (c) Shear strains at interfaces

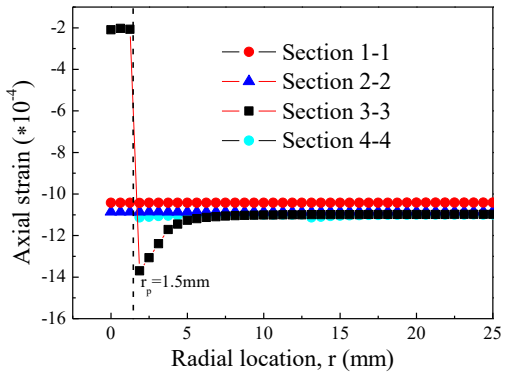

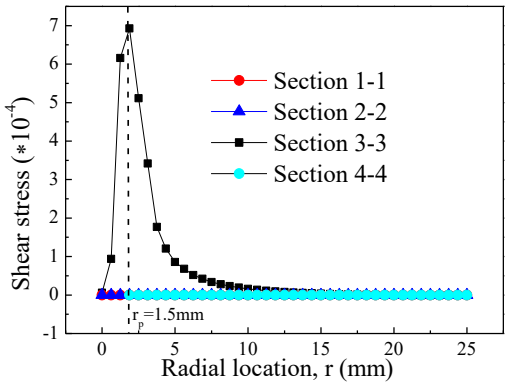

(d) Axial strains at various cross sections (e) Shear strains at various cross sections

Fig. 5 Strain field and distribution

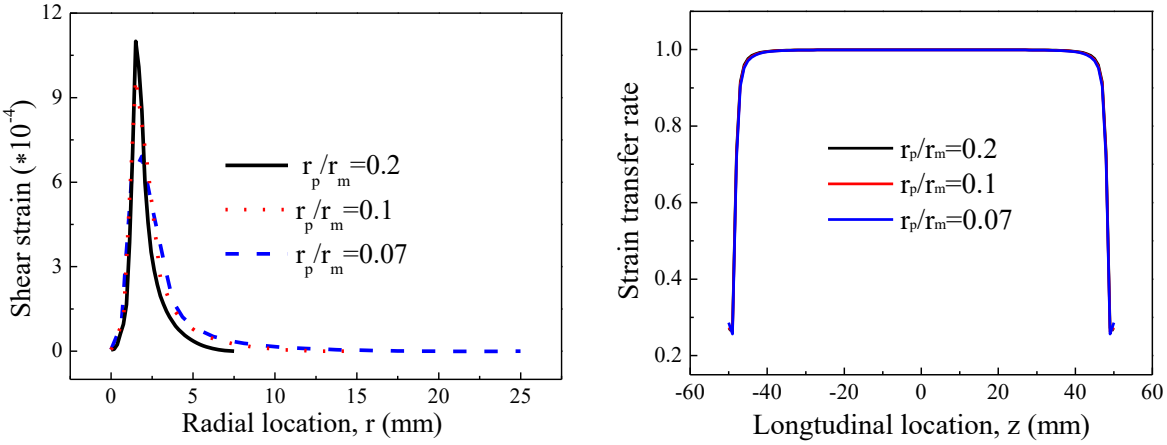

(a) Shear strain at Section 3-3 (b) Strain transfer rate

Fig. 6 Effects of r_p/r_m ratio on strain distribution and transfer rate

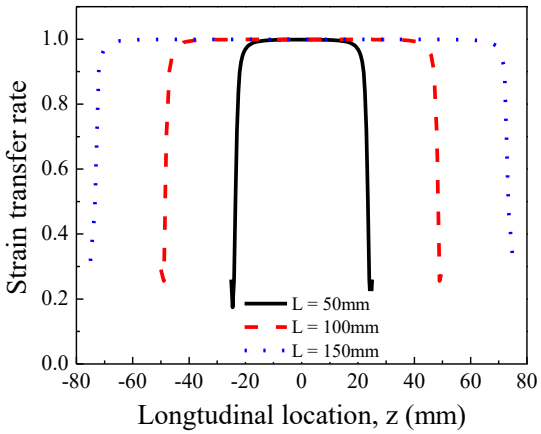

Fig. 7 Effect of sensor package length on the distribution of strain transfer rate

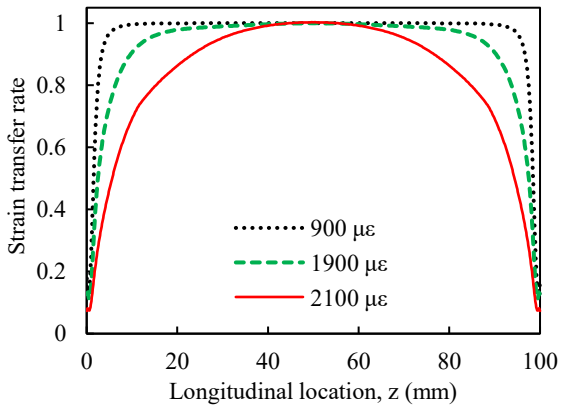

Fig. 8 Effect of loading on the distribution of strain transfer rate: *L=100 mm* and $r_p/r_m=0.07$

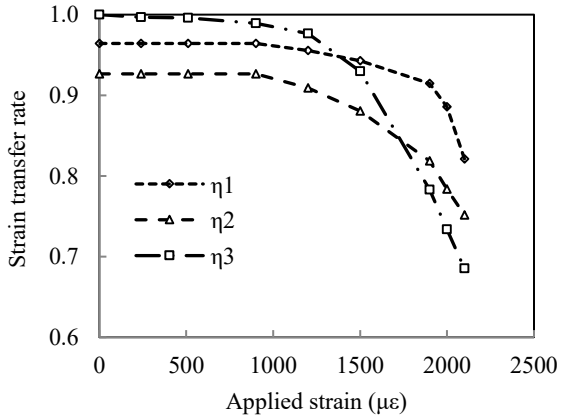

Fig. 9 Strain transfer rate as a function of applied strain

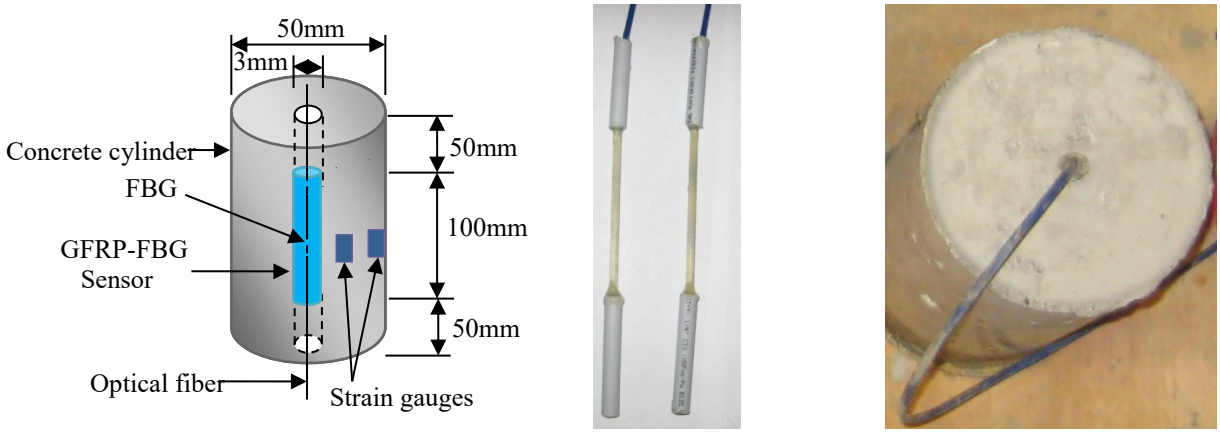

(a) Schematic view (b) GFRP-packaged FBG sensors (c) Representative specimen

Fig. 10 Test specimen and instrumentation

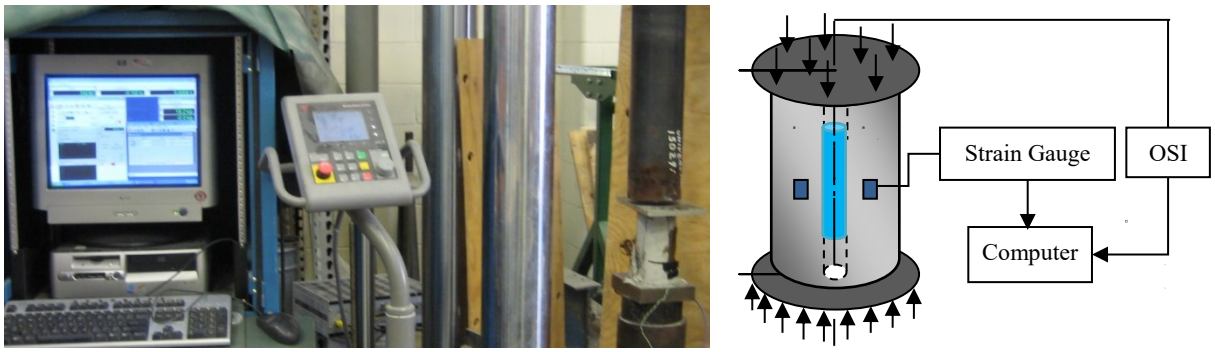

(a) One specimen tested to failure (b) Schematic view

Fig. 11 Experimental setup

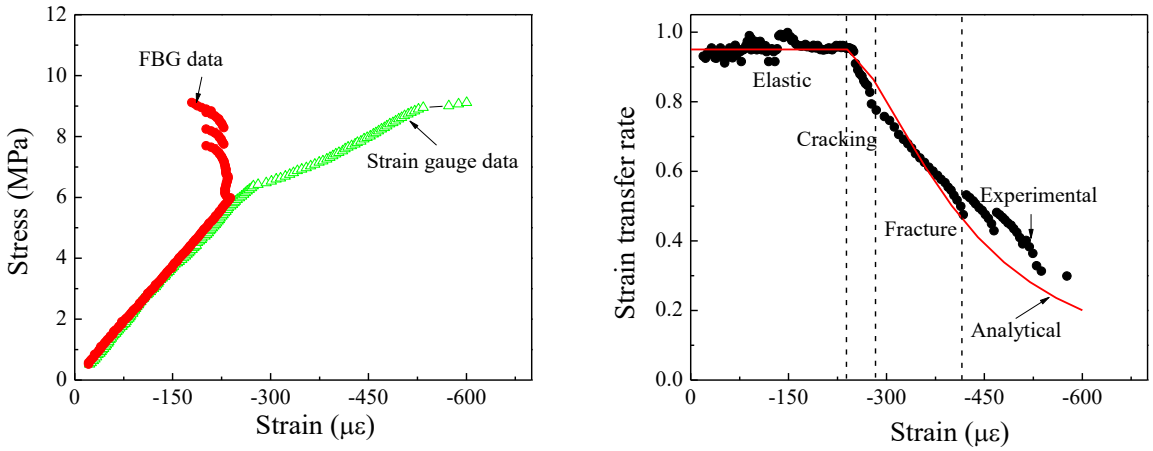

(a) Stress-strain relations (b) Analytical vs. experimental strain transfer rate

Fig. 12 Constitutive law and strain transfer rate of cylinder specimen #1

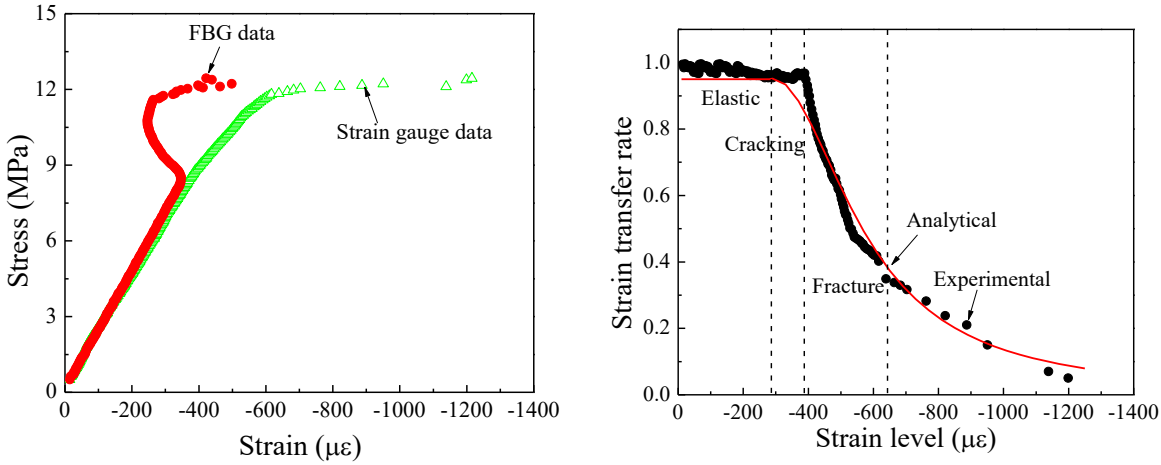

(a) Stress-strain relations (b) Analytical vs. experimental strain transfer rate

Fig. 13 Constitutive law and strain transfer rate of cylinder specimen #2

(a) Crack initiation (b) Failure mode (c) Tested specimens

Fig. 14 Concrete behavior of the tested specimens